

HST Imaging in the Chandra Deep Field South: I. Multiple AGN Populations

Ethan J. Schreier, Anton M. Koekemoer, Norman A. Grogin

Space Telescope Science Institute, 3700 San Martin Drive, Baltimore, MD 21218, USA

R. Giacconi, R. Gilli, L. Kewley, C. Norman

Department of Physics and Astronomy, Johns Hopkins University, Baltimore, MD 21218, USA

G. Hasinger

Astrophysikalisches Institut, An der Sternwarte 16, Potsdam 14482 Germany

P. Rosati

European Southern Observatory, Karl-Schwarzschild-Strasse 2, Garching, D-85748, Germany

A. Marconi, M. Salvati

Osservatorio Astrofisico di Arcetri, Largo E. Fermi 5, 50125 Firenze, Italy

P. Tozzi

Osservatorio Astronomico di Trieste, Via G. B. Tiepolo 11, 34131 Trieste Italy

ABSTRACT

We present preliminary results from imaging three *HST*/WFPC2 fields in *V* and *I* within the Chandra Deep Field South (CDFS). *HST*'s sensitivity and resolution are sufficient to reveal optical counterparts for 24 of the 26 CDFS X-ray sources detected in the 300 ksec X-ray catalog and to determine the morphologies of most of these. We find that the X-ray sources comprise two apparently distinct populations of optical candidates: one optically faint ($I \gtrsim 24$) with $V-I$ colors consistent with the $I > 24$ field population; the other significantly brighter ($I \lesssim 22$) with colors redder than the $I < 22$ field population. More than 2/3 of the X-ray source counterparts are resolved galaxies. The brighter sources are mostly AGN, based on their high X-ray luminosity. The optically resolved sources in the brighter population have a very narrow range of $V-I$ color and appear to be a mix of both late and early type morphologies at low to moderate redshift. We show that the second population, with fainter optical counterparts, can be explained as higher redshift Type 2 AGN.

1. Introduction

Galaxy formation and evolution are fundamental topics in astrophysics today. *HST*'s high resolution has been particularly important in opening up these fields and framing the questions: How did large scale structure initially form? What is the role of hierarchical mergers? What is the role of the massive central black holes (BHs) which now appear to be found in most nearby galaxies (Magorrian et al. 1998)?

Just as high-resolution optical and near-IR observations are essential to the study of galaxy formation and evolution, X-ray astronomy has been key to the study of active galactic nuclei (AGN). We now commonly explain AGN via accretion onto massive black holes, with the difference between Type 1 and Type 2 AGN explained via an obscuring torus in the standard unified model (e.g., Urry & Padovani 1995). We further explain the cosmic X-ray background (XRB) via integrated emission from AGN. During the last few years, deep soft (ROSAT) and hard (ASCA, BeppoSAX) X-ray surveys have provided essential information on the evolution of AGN and on the origin of the XRB. About 80% of the $0.5 - 2$ keV background was resolved into discrete sources by ROSAT (Hasinger et al. 1998), and most of these sources were identified as AGN (Schmidt et al. 1998). These AGN are typically broad line QSOs or Type 1 Seyferts, to be expected given ROSAT's sensitivity to soft X-rays and thus unobscured AGN. The deep ROSAT surveys also sampled the low end of the luminosity function of AGN at high- z , discovering strong *density* evolution (Hasinger et al. 1999, Miyaji et al. 2000). This is thought to be a consequence of the larger rate of interactions and distorted/irregular morphologies at high- z (Lilly et al. 1998, Abraham et al. 1999). Chandra is now extending these results to lower fluxes and to harder X-rays (cf. Giacconi et al. 2001a, Hornschemeier et al. 2001, Mushotzky et al. 2000, Giacconi et al. 2001b, Tozzi et al. 2001).

Nonetheless, the physical nature of the relation between AGN evolution and galaxy evolution is unknown. Recent evidence for the existence of this relationship comes from the strong correlation observed between BH mass and host galaxy bulge velocity dispersion (Gebhardt et al. 2000, Ferrarese & Merritt 2000). But the very basic question of whether nuclear activity drives galaxy evolution or vice versa is still open.

Answering these questions requires observing obscured and unobscured AGN *and* their hosts, as a function of redshift. The combination of *HST* and Chandra provides the potential to first detect AGN via their X-ray emission, and then to study their optical host galaxies with *HST*. This permits studying the effect of environment on AGN and their evolution, and perhaps the effect of the AGN on their environments. The immediate questions are: 1) are tidal interactions and/or distorted morphologies more prevalent in AGN hosts than in field galaxies? 2) are host galaxy characteristics correlated with AGN characteristics like flux and hardness (i.e., obscured vs. non-obscured), and do these correlations change with z ? 3) can

we confirm the unified model at high z ? 4) can we measure AGN luminosity vs. expected Eddington luminosity as a function of z (by estimating BH masses via follow-up velocity dispersion measurements of host bulges)?

In this paper we show the first results from *HST* imaging in the Chandra Deep Field South (hereafter CDFS; Giacconi et al. 2001a). These optical observations represent a pilot project to establish the feasibility of studying faint X-ray source host galaxy morphologies. Although the X-ray data have not yet been fully analyzed, and only preliminary optical spectra and redshifts are available, we report several new results from the preliminary analyses. We confirm that we can readily resolve structure in optical candidates for the CDFS sources.

In Section 2 we describe the observations and data reduction and in Section 3, the optical source extraction. In Section 4, we describe the characteristics of the optical counterparts of the X-ray sources, and in Section 5 we discuss the results. Throughout this paper we assume a cosmology with $\Omega_\Lambda = 0.7$, $\Omega_M = 0.3$, $H_0 = 70 \text{ km s}^{-1} \text{ Mpc}^{-1}$.

2. *HST*/WFPC2 Observations of the Chandra Deep Field South

The optical observations presented here comprise three *HST* Wide Field Planetary Camera 2 (WFPC2) fields, located in the central regions of the $\sim 0.1 \text{ deg}^2$ Chandra Deep Field South (CDFS). The CDFS is centered at RA 03 32 28.0, Dec $-27^\circ 48' 30''$ (J2000). It was selected for this very deep X-ray survey because of its high galactic latitude, lack of bright stars, low $N(\text{H})$, and accessibility to VLT and Gemini. The initial published X-ray results (Giacconi et al. 2001a) were based on a total exposure of 126 ksec. Our current analysis of the *HST* observations uses the X-ray catalog and results based on 300 ksec of exposure (Tozzi et al. 2001). A total of about 940 ksec of Chandra data have by now been taken on the CDFS (cf. Giacconi et al 2001b). A forthcoming paper will extend our analysis to all X-ray sources seen in the full 940 ksec CDFS exposure and will also present more detailed quantitative morphology analyses for the optical counterparts.

Our *HST*/WFPC2 exposures were taken with the F606W (hereafter V) and F814W (hereafter I) filters (Table 1). Five orbits were allocated to each field: 2 orbits in V and 3 in I . The data were taken in July 2000 using the “dither” mode, which involves offsetting the telescope by integral plus 1/2-pixel increments to both improve the sampling of the *HST* PSF and ameliorate the effect of bad pixels. The data underwent standard WFPC2 pipeline calibration, after which the individual dithered images of each field were combined into a single $0''.05/\text{pixel}$ image for each filter using the *drizzle* software (Fruchter & Hook,

2001) in the IRAF/STSDAS *dither* package. The data were calibrated in the VEGAMAG photometric system, using the current best values for the zero points (cf. *HST*/WFPC2 Instrument Handbook, V.5, 2000).

Figure 1 shows color images of each of the three WFPC2 fields of view, with blue representing F606W V , red representing F814W I , and green a mean image of the two. The three WFPC2 fields include a total of 26 X-ray sources listed in the 300 ksec Chandra catalog. Figure 2 shows the three WFPC2 fields of view overlaid on a map of the 300 ksec X-ray sources, coded for intensity, as detected by Tozzi et al. (2001) in their 0.5 – 7 keV detection band. Since we chose HST pointings to optimize the number of X-ray sources observed, the density of sources in our fields is higher than would be expected for random WFPC2 fields. Note that Tozzi et al. find 197 sources in their 0.104 deg^2 field, with clustering on scales up to $100''$. Our 26 sources in a total area of $\approx 17 \text{ arcmin}^2$ represents ~ 3 times the average source density. Figure 3 is a collage of $20'' \times 20''$ *HST* $V+I$ image sections, centered on each Chandra source in our fields and overlaid with the 0.5 – 7 keV X-ray contours from the 300 ksec data (Tozzi et al. 2001). We show, for reference, the expected *CXO* point source response size (FWHM) at each source location.

3. Optical Source Extraction and Photometry

We first created a detection image for each WFPC2 field by adding the V and I images. We then extracted sources with the SExtractor program (version 2.1.6; Bertin & Arnouts 1996). In light of the correlated noise and the ≈ 3 -pixel FWHM in the $0''.05/\text{pixel}$ drizzled images, we adopted conservative SExtractor detection criteria: 10 contiguous pixels at ≥ 1.5 times the RMS (≈ 2.3 counts in the WFC regions and ≈ 5.8 counts in the PC regions). For a source with equivalent counts in each filter ($V-I = 1.2$), this corresponds to a WFC detection limit of $I \leq 28.2$ and $\mu_I \leq 24.2 \text{ mag arcsec}^{-2}$. The corresponding limits for the PC are $I \leq 27.2$ and $\mu_I \leq 23.2 \text{ mag arcsec}^{-2}$.

We ran SExtractor twice for each field using a single detection image as described above, but performing the photometry separately on the V and I images. This ensures that the source pixels are identically matched between the two filters. Our resulting optical source catalog contains 3834 objects among the three fields. We plot their I magnitudes and $V-I$ colors (based on the SExtractor MAG.BEST parameter) as the small dots in Figure 4. These magnitudes do not include correction for the WFPC2 charge-transfer inefficiency (Whitmore, Heyer, & Casertano 1999 and references therein), which we expect to be $< 0.03 \text{ mag}$ given the appreciable background in our exposures.

We assessed the catalog completeness as a function of magnitude by repeating the source extraction procedure after adding simulated point sources to the image using the IRAF task *mkobjects* in the *ARTDATA* package. To avoid overcrowding the images, we only added 150 simulated objects per WFC region and 50 objects per PC region, iterating to improve the statistics. We estimate that our catalog is complete to $I \approx 26.4$, where our point-source recovery rate has fallen to $\approx 90\%$ for objects with the median color $V-I \approx 1.2$. We plot this completeness limit as a function of I magnitude and $V-I$ color on Figure 4 (dotted curve). The simulated point-source recovery also gives us an independent estimate of the SExtractor photometric errors. In the figure we show 1σ photometric error bars for objects with the median colors at $I = 23, 24, 25$, and 26 . For brighter simulated sources, both I and $V-I$ are recovered to better than 0.03 mag, the level at which we expect unmodeled systematic errors (e.g., charge-transfer inefficiency) to contribute.

4. Optical Counterparts of X-ray Sources

Each of our fields has $7 - 10$ objects clearly associated with CDFS 300 ksec cataloged sources. We registered each WFPC2 mosaic independently to the *CXO* frame by subtracting the error-weighted median offset to these *CXO* sources. We list the *CXO* coordinate IDs of these counterparts in Table 2, along with the coordinate offsets from their associated *HST* sources. The mean deviation of the 24 registered *HST* coordinates about the *CXO* source positions is $0''.4$, with a maximum offset of $1''.2$. This is broadly consistent with the *CXO* positional uncertainties, which range from $0''.1$ to $0''.5$ (Tozzi et al. 2001). A detailed analysis of the CDFS X-ray source positions with respect to the optical galaxy positions — in particular whether they all lie at the centers of the galaxies — will be valuable in helping determine the nature of the X-ray emission (cf. Brandt et al. 2001). This will await the analysis of the 940 ksec data, where the expected greater number of sources will provide better registration between the X-ray and optical fields, and where the better counting statistics will improve the individual X-ray source positions.

There are only two CDFS 300 ksec sources (IDs J033204.5–274644 and J033205.4–274644) within our three WFPC2 fields more than $2''$ away from the nearest source in our catalog, 5 times the mean offset for the rest of the sample. Both sources are on the PC in field CDFS2 and have 3σ upper limits on (V, I) of $(26.8, 25.5)$ based on $0''.5$ -radius apertures centered on the *CXO* coordinates. If these sources had fallen on one of the WFCs rather than the PC, the detection upper limits would have been ≈ 1 mag fainter.

For all 26 *CXO* sources in our fields, we list in Table 2 the V and I magnitudes (or 3σ upper limits) from this study, as well as the derived *CXO* fluxes in the bands $0.5 - 2$ keV

(column F_{XS}) and $2 - 10$ keV (column F_{XH}), and the X-ray hardness ratio HR from Tozzi et al. (2001). We also tabulate the hardness ratio $HR \equiv (H - S)/(H + S)$, where H and S are the net counts in the hard ($2 - 7$ keV) and soft ($0.5 - 2$ keV) band, respectively. For comparison, the hardness ratio of the X-ray background, with photon index $\Gamma \approx 1.4$, is $HR \approx -0.38$ (Tozzi et al. 2001). In Table 2 we also include preliminary estimates for the redshift and spectral classification for many of the optical counterparts based on recent VLT/FORS spectroscopy by Hasinger et al. (2001). Because emission-line ratio diagnostics were not yet available to discriminate between Type 2 AGN and starburst spectra, we conservatively label all such candidates as narrow emission-line galaxies (NELGs).

We find that the SExtractor star/galaxy separation is reliable to $V \lesssim 25.4$, substantially fainter than most CXO counterparts. Values of the V-band SExtractor STELLARITY parameter η_V span the range $0 - 1$, with clearly resolved sources having $\eta_V \lesssim 0.2$ and clearly unresolved sources having $\eta_V \gtrsim 0.8$. Fifteen of the 24 optical counterparts to the X-ray sources are clearly resolved ($\eta_V < 0.2$). Most of these resolved sources are sufficiently extended to permit detailed examination and classification as elliptical, spiral, or irregular galaxies — we note their optical morphology in Table 2. Of the remainder, seven are clearly unresolved, and two are too faint for reliable star/galaxy separation (listed as “indeterminate” morphology in Table 2).

For the clearly extended sources, we also fit surface brightness profiles with the IRAF/STSDAS isophotal analysis package, ISOPHOTE. The package’s contour fitting task *ellipse* takes an initial guess for an isophotal ellipse, then steps logarithmically in major axis. At each step it finds the optimal isophotal ellipse center, ellipticity, and positional angle. Prior to the ellipse fitting, we use the task *imedit* to mask foreground stars, neighboring galaxies, etc., near the galaxies of interest, and ignore masked pixels in the fitting. The surface brightness profiles corroborate the qualitative morphology assessment obtained by visual inspection. The quantitative results from the surface photometry will be presented in the forthcoming paper.

In Figure 4, we flag the optical counterparts of the X-ray sources among the full-field color-magnitude diagram with symbols according to their optical morphology: circles represent resolved early type galaxies (types S0 and earlier); squares are resolved later type galaxies (types Sa and later); stars represent clearly unresolved sources; and triangles are objects of indeterminate morphology.

5. Discussion

There is a readily apparent dichotomy in the color magnitude distribution of the optical counterparts of the X-ray sources: a brighter group with $I \sim 17.8 - 22.7$, and a fainter group with $I \sim 24.2 - 25.3$. The fainter group (containing only five sources) is consistent in its color distribution with the field galaxy population. The other group is both significantly brighter and significantly redder, on average, than the population of field sources.

Further, those optically bright X-ray sources that are extended in our *HST* images (those indicated by squares and circles in Figure 4) appear redder than the rest of the bright sources. This subset of bright extended sources occupies a narrow range of color, $V-I \sim 1.7 - 2.2$, while spanning a magnitude range $I \sim 19 - 22.7$. There is also a suggestion that the Chandra-detected late type galaxies are optically fainter than the corresponding early-type galaxies.

The fact that the X-ray sources with resolved optical candidates appear to occupy two different regions of color-magnitude space strongly suggests that we are seeing two (or more) different populations of sources. We note that the faint limit ($I \sim 23$) of the brighter population is well above our completeness limit, and that the distributions of these sources in both magnitude and color are significantly different from the field population distributions. In Figure 6, we plot histograms of the number of sources vs. color for the X-ray source counterparts (solid) and the field sources (dotted). The top set of histograms includes sources at all magnitudes, the bottom is limited to sources with $I < 23$. The redder color of the X-ray emitting galaxies is obvious, even when we limit the field sample to the brighter sources. A Kolmogorov-Smirnov (K-S) test rules out a common underlying color distribution at the 4σ level.

The color-magnitude diagram also shows a far greater incidence of X-ray counterparts for the optically brighter sources than for the fainter sources — 16 *CXO* detections among the 195 *HST* sources with $I \leq 22$, in contrast to 5 detections among the 2060 sources with $26 \leq I \leq 23$. We suggest that the brighter population is spatially relatively sparse, since the sources are observed well above the optical detection limit. Furthermore, the X-ray luminosities estimated from the available preliminary redshifts suggest that these are predominantly AGN: 11 of 16 optically bright sources have X-ray luminosities $L(0.5 - 10 \text{ keV}) > 10^{43} \text{ erg s}^{-1}$, and 5 have luminosities in the range $10^{42} - 10^{43} \text{ erg s}^{-1}$, likely Type 2 AGN and/or starburst galaxies. The fact that the AGN are associated, on average, with redder galaxies could suggest the presence of dust associated with mergers in AGN hosts.

The X-ray emitting galaxies in the optically fainter group represent a small fraction of the field galaxies, but their colors, on the other hand, are near the average for the field

population. Their optical fluxes are not much above our detection limits, and we suggest that these could well represent the high X-ray intensity tip of a much larger population of sources.

In Figure 5, we overlay predicted templates for elliptical, spiral, and irregular/starburst galaxies on the same color-magnitude diagram, motivated by similar comparisons carried out previously, for example in the HDF-N (Williams et al. 1996). The templates are taken from Coleman et al. (1980), with fluxes computed through the *HST* filter bandpasses after applying a range of redshifts, and assuming $\sim L_*$ luminosities for each galaxy class. We also plot a Type 1 AGN track (for a QSO of $M_B = -24$), assuming the fluxes are dominated by the flat-spectrum nuclear component. For the X-ray counterparts, we use the same symbols as in Figure 4 to distinguish between ellipticals, spirals, unresolved and indeterminate optical classifications. We further code for the intensity and hardness ratio for the X-ray sources, with size being proportional to X-ray flux, and darker shading indicating harder X-ray spectra. We see from the tracks that the bright, extended population of objects in the narrow color range $V-I \sim 1.9$ are consistent with early-type galaxies and spirals at low to moderate redshifts ($z \sim 0.5 - 1.2$). Our optical data confirm that we see both early-type and spiral morphologies for these objects, and those preliminary redshifts which are available (Hasinger et al. 2001) are also consistent with the expected range (cf. Table 2). The range of apparent magnitudes ($I \sim 19 - 23$) is consistent with these objects being $\sim L_*$ galaxies at these fairly moderate redshifts. We note that the spirals in this sample are generally fainter than the ellipticals, in agreement with the predictions from the redshifted tracks. Finally, we find that the unresolved sources generally fall between the elliptical/spiral template tracks and those of the pure Type 1 AGN spectrum, suggesting that these objects are Type 1 AGN with smaller, varying admixtures of host galaxy contributions to the total flux. These point-like sources are also bluer, for a given magnitude, than the resolved sources. The colors of these objects are similar to starbursts, however their X-ray luminosities are higher than those expected for typical starbursts, thus we conclude that they are more likely to be AGN.

We have already noted that the color distribution of the fainter group is consistent with that of the field galaxy population. The predicted galaxy tracks suggest that the field population at these magnitudes consists of irregulars and more distant spirals and starbursts. We may also be starting to see the faint blue population of galaxies that has been previously discussed in the context of the HDF-N (e.g., Mobasher et al. 1996, Phillips et al. 1997). The X-ray sources in this optically faint population have high F_X/F_{opt} and are likely to be distant AGN, as discussed below.

To further explore the nature of the two populations, we have simulated the expected number counts and color-magnitude distribution for various classes of objects. We have

used published template SEDs, luminosity functions and general evolution models for ellipticals, spirals, and starbursts, as well as Type 1 and Type 2 AGN. For ellipticals, spirals and starburst/Im galaxies we used templates from Coleman et al. (1980) at optical wavebands, combined with multiwaveband data from Schmitt et al. (1997) extending up to X-ray energies. For Type 1 AGN we used composite spectra from Cristiani & Vio (1990) supplemented again by Schmitt et al. (1997) for X-ray energies, while our Type 2 AGN template was taken from Della Ceca et al. (2000). For the non-active galaxies we adopted the same luminosity function and evolution as determined by Loveday et al. (1992), while for the AGN we used the Type 1 luminosity function and evolution recently determined by Boyle et al. (2000). We applied the Type 1 LF to the Type 2 AGN by assuming that the ratio of Type 1/2 remains constant with redshift, is determined by a torus with opening angle 60° , and that the emission from the torus is isotropic at $60\ \mu\text{m}$ (thus normalizing the SEDs at this frequency). These are all fairly extreme oversimplifications, and we will present more detailed modelling in Koekemoer (2001) in the context of the entire set of sources from the 940 ksec catalog. For the moment, however, we note that the results are not dramatically sensitive to details such as the precise ratio of Type 1/2 (and whether it varies with redshift). We simulated the expected fluxes in the optical using the filter throughput curves for *HST*/WFPC2, and similarly the Chandra fluxes in the soft and hard bands were simulated using the available sensitivity data for ACIS-I as a function of energy.

In Figure 7, we present the histogram of the I magnitude distribution of the observed optical counterparts of the Chandra sources, along with predicted curves (to be discussed in more detail our forthcoming paper) for ellipticals, spirals, starbursts, and AGN, based on the above models, an area of sky corresponding to our three WFPC2 fields (a total of $17.1\ \text{arcmin}^2$), and detection thresholds for the 300 ksec Chandra X-ray data as described by Tozzi et al. (2001). We also show the sum of the contributions from each type.

It is clear from the predictions in Figure 7 that the majority of the X-ray source optical counterparts are expected to be relatively bright, as observed. The group includes ellipticals, spirals, starbursts, and Type 1 and Type 2 AGN. More interesting, the optically faint population ($I \gtrsim 24 - 25$) of X-ray source counterparts is expected to consist only of higher-redshift Type 2 AGN ($z \sim 2$). Furthermore, the models suggest that these would be softer than their lower-redshift counterparts, by virtue of the predicted higher redshifts causing more X-ray emission to be shifted into the soft band. This prediction agrees with the observed X-ray hardness ratios: the optically faint sources are not as hard in the X-rays as the optically brighter ones. Moreover, the one object in this faint group for which we have a preliminary redshift (J033208.3–274153) is a NELG with $z = 2.45$, leading to an X-ray luminosity estimate of $\approx 3 \times 10^{43}\ \text{erg s}^{-1}$, in the rest frame energy range of $1.7 - 35\ \text{keV}$. This is substantially brighter than expected for a starburst, and is likely a distant type 2

AGN.

In Figure 8, we plot X-ray vs. optical flux of the CDFS sources, for the hard and soft X-ray bands separately. The population of optically brighter, resolved sources lies along a line of constant F_X/F_{opt} with a relatively low value compared with the other CDFS sources. As stated earlier, the lack of objects at lower F_X/F_{opt} , i.e. in the lower left corner of the plot, is not an observational bias. As we move to even lower values of F_X/F_{opt} , we would eventually reach levels consistent with X-ray emission from normal galaxies.

The unresolved sources tend to have higher F_X/F_{opt} , reflecting the relative dominance of AGN emission over host galaxy contribution over these mostly Type 1 AGN. Note also that the optical non-detections (lower right) are consistent with the high F_X/F_{opt} ratio of the faint population.

For fainter X-ray flux detection limits, our models predict a substantial increase in the number of optically faint counterparts, the majority of which should be obscured AGN at reasonably high redshifts of $z \gtrsim 1.5 - 2.5$ (cf. Figure 7). While we can also expect to see additional objects in the “gap” between the two populations, the “double peak” in the source count histogram should persist – the bright population of unobscured AGN and starbursts, and the fainter population of distant, obscured AGN, with the peak of the faint population being considerably broader than that of the bright population.

Although few of the *CXO*-detected galaxies show obvious signs of strong disruption or disturbances (e.g., J033213.3–274241), most have nearby companions ($\lesssim 5''$) and at least a few reside within apparent compact groups (e.g., J033208.1–274658, J033233.1–274548). If galaxy activity and X-ray emission were correlated with local environment, e.g., from interaction-induced star formation and/or feeding of a central BH, we might expect to see more near neighbors around the *CXO*-detected galaxies than typical for the field. We investigate this by determining the number of companion galaxies ($\eta_V < 0.2$), with $I \leq 23$, within $8''$ of each $I \leq 23$ galaxy in our source catalog. For our adopted cosmology, $8''$ corresponds to a projected distance of 50 kpc at $z \approx 0.6$, typical of the *CXO*-detected galaxies at $I \leq 23$ (cf. Table 2). Figure 9 shows the histogram of this near-neighbor distribution for the 12 *CXO*-detected $I \leq 23$ galaxies (solid line) and for the full sample of the 328 galaxies with $I < 23$ (dotted line). Although the chi-square test gives a high probability (0.49) of the null hypothesis that the two histograms are consistent with a single nearest-neighbor distribution function, the analysis would greatly benefit from enlarging the *CXO*-detected population with wider optical coverage (and with the 940 ksec CDFS data).

We have verified that our selection of *HST*-observed sources is, on average, representative of the full catalog of 300 ksec CDFS sources in terms of X-ray flux and hardness. Figure 10

shows the hardness ratio versus $0.5\text{--}10$ keV flux for the full 300 ksec catalog of X-ray sources, overlaid with our standard symbols for the optical counterparts. We see that the optically resolved counterparts span a broad range of the X-ray parameter space. We also note that the unresolved counterparts appear, on average, softer in the X-rays, reflecting a lack of obscuration. As there are not yet accurate redshifts for half of our optical counterparts, we cannot make definitive statements based on intrinsic luminosities.

6. Conclusion

Summarizing our initial results, we find that with only two exceptions, all X-ray sources detected by Chandra in the initial 300 ksec exposure that lie in our WFPC2 FOVs have apparent optical counterparts within ~ 0.5 arcsec, to our limiting magnitude of $V \sim 28.4$. The majority of the candidates are resolved galaxies, and many are at low to moderate redshifts.

There appear to be two distinct populations of optical counterparts for the X-ray sources: a brighter population, with $I \sim 17.8\text{--}22.7$; and a fainter population, with $I \sim 24\text{--}25$. The brighter population is both significantly brighter and significantly redder on average than the population of field sources. The fainter population (only five sources) is consistent in its color distribution with the field galaxy population. There is no significant difference in X-ray hardness between the groups, although in each group, the harder sources appear marginally redder.

The optically bright X-ray sources identified with resolved galaxies are redder than the overall population of bright sources and lie in a narrow range of color: $V - I \sim 1.7\text{--}2.2$, over a magnitude range of $I = 19\text{--}22.7$. These values are consistent with $\sim L_*$ galaxies at moderate redshifts of 0.5 to 1.2, comparable to the range of preliminary redshifts already measured (cf. Table 2). The high X-ray luminosities suggest that most of these harbor AGN. The redder colors of the *CXO* optical counterparts further imply that these AGN hosts are dusty, as might be expected if mergers were associated with nuclear activity. The spirals in this sample are also generally fainter than the ellipticals, as expected from the comparison of their colors and luminosities with predicted galaxy templates. The bright population of galaxies lies well above our optical detection threshold, suggesting that these comprise a relatively sparse, volume-limited and not flux-limited population.

The optically faint group of *CXO* sources is consistent in color distribution with the field galaxy population. These sources are likely to be high redshift Type 2 AGN ($z \sim 2$). They appear softer than the nearer Type 2 AGN because their unobscured hard X-ray emission is

substantially redshifted into the *CXO* soft band. We predict that at still fainter X-ray flux limits, we will find substantially more of the faint optical counterparts, but few additional members of the resolved brighter population.

In conclusion, we note that these *HST* observations cover only some 7.5% of the full-depth 300 ksec CDFS area (Tozzi et al. 2001). More and deeper observations should be undertaken. Our current results suggest that *HST*/WFPC2 or ACS exposures of the CDFS at $\mu_I \sim 24 - 25$ mag arcsec $^{-2}$ can easily resolve the optical counterparts of many more of the Chandra sources in our fainter population. This should represent a complete sample of X-ray selected AGN host galaxies out to $z \sim 2$, at or beyond the expected peak in AGN density evolution. *HST*/NICMOS *K*-band observations and the eventual *SIRTF* Great Observatories Origins Deep Survey (GOODS) of this field will provide valuable infrared diagnostics of the AGN vs. starburst contributions, in conjunction with additional ground-based optical and near-IR spectroscopy.

These initial results already demonstrate the ability of *HST*, in a relatively modest amount of observing time, to readily detect the host galaxies of distant, low-luminosity AGN and to reveal their morphology. We will present more quantitative morphology results, detecting color gradients and distinguishing unresolved AGN emission from the host galaxy emission, in a forthcoming paper that will include the optical counterparts from the full 940 ksec CDFS exposure.

We gratefully acknowledge the award of *HST* Director’s Discretionary time in support of this project. We also acknowledge support for this work which was provided by NASA through GO grants GO-08809.01-A and GO-07267.01-A from the Space Telescope Science Institute, which is operated by AURA, Inc., under NASA Contract NAS 5-26555. We thank the referee for very useful suggestions.

REFERENCES

- Abraham, R. G., Ellis, R., Fabian, A., Tanvir, N., & Glazebrook, K. 1999, MNRAS, 303, 641
- Bertin, E. & Arnouts, S. 1996, A&AS, 117, 393
- Biretta, J. A. et al. 2000, WFPC2 Instrument Handbook, Version 5.0 (Baltimore: STScI)
- Brandt et al. 2001, AJ, in press (astro-ph/0102411)
- Boyle, B. J., Shanks, T., Croom, S. M., Smith, R. J., Miller, L., Loaring, N., & Heymans, C. 2000, MNRAS, 317, 1014

- Coleman, G. D., Wu., C.-C., & Weedman, D. W. 1980, *ApJS*, 43, 393
- Ferrarese, L. & Merritt, D. 2000, *ApJ*, 539, 9
- Fruchter, A. S. & Hook, R. 2001, *PASP*, submitted
- Gebhardt, K., Kormendy, J., Ho, L. C., Bender, R., Bower, G., Dressler, A., Faber, S. M., Filippenko, A. V., Green, R., Grillmair, C., Lauer, T. R., Magorrian, J., Pinkney, J., Richstone, D., & Tremaine, S. 2000, *ApJ*, 539, 13
- Giacconi, R., Rosati, P., Tozzi, P., Nonino, M., Hasinger, G., Norman, C., Bergeron, J., Borgani, S., Gilli, R., Gilmozzi, R., & Zheng, W. 2001a, *ApJ*, in press (astro-ph/0007240)
- Giacconi, R., Zirm, A., Wang, J. X., Rosati, P., Tozzi, P., Gilli, R., Gilmozzi, R., Hasinger, G., Kewley, L., Nonino, M., Bergeron, J., Borgani, S., Grogin, N., Kellermann, K., Koekemoer, A., Schreier, E., Shaver, P., Zheng, W. & Norman, C. 2001b, in preparation
- Hasinger, G., Burg, R., Giacconi, R., Schmidt, M., Truemper, J., & Zamorani, G. 1998, *A&A*, 329, 482.
- Hasinger, G., et al. 1999, in "Highlights in X-ray Astronomy", MPE report 272, 199 (astro-ph/9901103)
- Hasinger, G., et al. 2001, in preparation
- Hornschemeier et al. 2001, *ApJ*, submitted (astro-ph/0101494)
- Koekemoer, A. M., et al. 2001, in preparation
- Lilly, S., Schade, D., Ellis, R., Le Fevre, O., Brinchmann, J., Tresse, L., Abraham, R., Hammer, F., Crampton, D., Colless, M., Glazebrook, K., Mallen-Ornelas, G., & Broadhurst, T. 1998, *ApJ*, 500, 75
- Loveday, J., Peterson, B. A., Efstathiou, G., & Maddox, S. J. 1992, *ApJ*, 390, 338
- Magorrian, J., Tremaine, S., Richstone, D., Bender, R., Bower, G., Dressler, A., Faber, S. M., Gebhardt, K., Green, R., Grillmair, C., Kormendy, J., Lauer, T. 1998, *AJ*, 115, 2285
- Maiolino, R., Salvati, M., Antonelli, L., Comastri, A., Fiore, F., Ghinassi, F., Gilli, R., La Franca, F., Mannucci, F., Risaliti, G., Thompson, D., & Vignali, C. 2000, *A&A*, 355, L47
- Miyaji, T., Hasinger, G., & Schmidt, M. 2000, *A&A*, 353, 25
- Mobasher, B., Rowan-Robinson, M., Georgakakis, A., & Eaton, N. 1996, *MNRAS*, 282, L7
- Mushotzky, R., Cowie, L. L., Barger, A. J., & Arnaud, K. A. 2000, *Nature*, 404, 459

- Phillips, A. C., Guzman, R., Gallego, J., Koo, D. C., Lowenthal, J. D., Vogt, N. P., Faber, S. M., & Illingworth, G. D. 1997 ApJ, 489, 543
- Risaliti, G., Marconi, A., Maiolino, R., Salvati, M. & Severgnini, P. 2001, A&A, submitted (astro-ph/0102427)
- Saunders, W., Rowan-Robinson, M., Lawrence, A., Efstathiou, G., Kaiser, N., Ellis, R. S. & Frenk, C.S. 1990, MNRAS, 242, 318
- Schmidt, M., Giacconi, R., Hasinger, G., Truemper, J., & Zamorani, G. 1998, in "Highlights in X-ray Astronomy", MPE report 272
- Schmitt, H. R., Kinney, A. L., Calzetti, D., & Storchi-Bergmann, T. 1997, AJ 114, 592
- Tozzi, P., Rosati, P., Nonino, M., Bergeron, J., Borgani, S., Gilli, R., Gilmozzi, R., Hasinger, G., Grogin, N., Kewley, L., Koekemoer, A., Norman, C., Schreier, E., Shaver, P., Szokoly, G., Wang, J. X., Zheng, W., Zirm, A. & Giacconi, R. 2001, ApJ, submitted (astro-ph/0103014)
- Urry, C. M. & Padovani, P. 1995, PASP, 107, 803
- Whitmore, B., Heyer, I., & Casertano, S. 1999, PASP, 111, 1559

Fig. 1.— (a) *HST* three-color images of each of the three WFPC2 fields in the Chandra Deep Field South, made by assigning red to *I*, blue to *V*, and green to the average of the two bands. North is to the top and East is to the left. This figure is for the CDFS1 field.

Fig. 1.— (b) As for Fig. 1a, but for the CDFS2 field.

Fig. 1.— (c) As for Fig. 1a, but for the CDFS3 field.

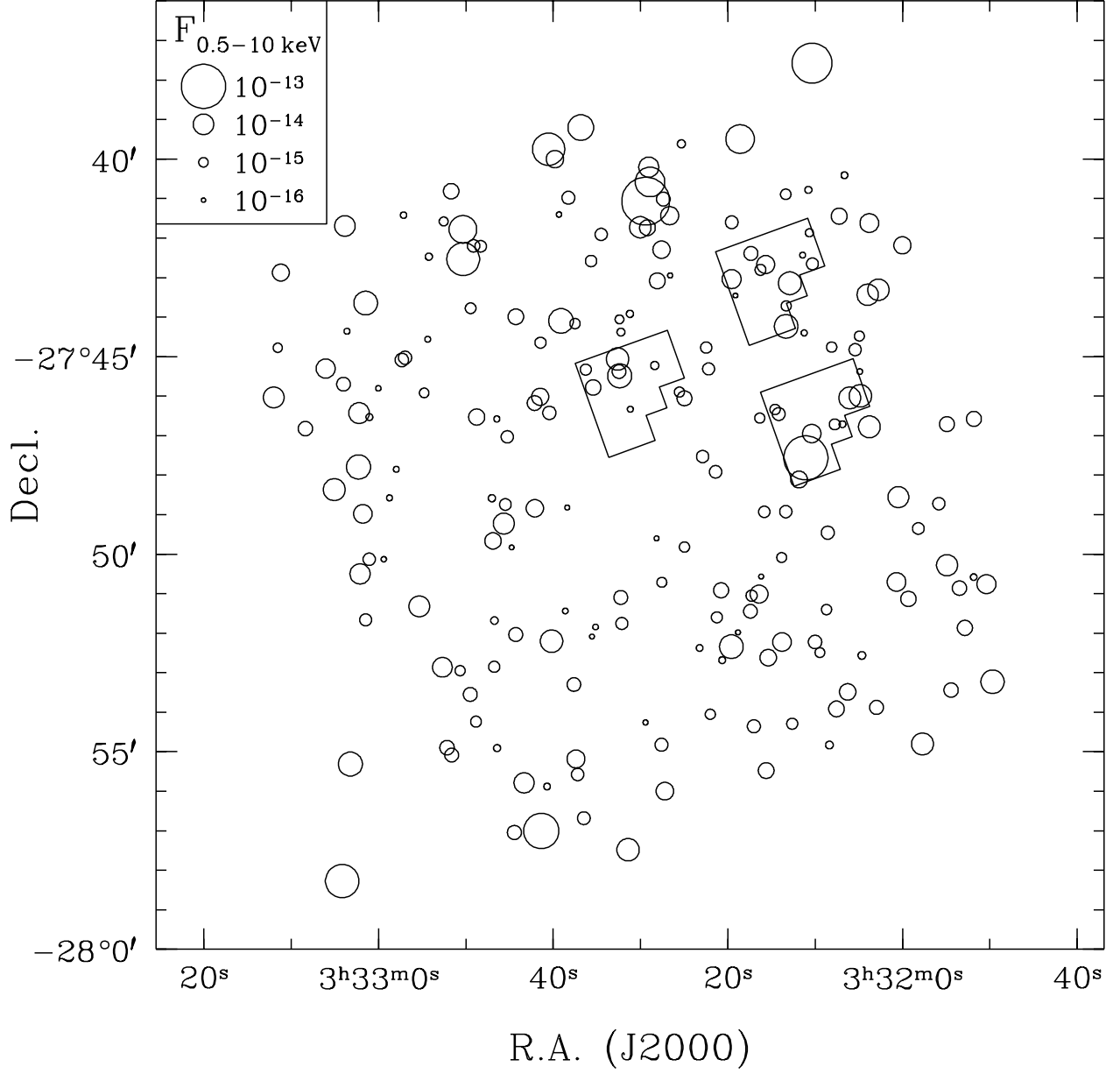


Fig. 2.— Map of all X-ray sources (open circles) detected in the 300 ksec *CXO* image of CDFS. The three *HST*/WFPC2 fields in this study are outlined by the chevrons toward the upper right. The *CXO* source fluxes (in $\text{erg s}^{-1} \text{cm}^{-2}$ at 0.5–10 keV) are denoted by symbol size, as indicated by the legend at the upper left.

Fig. 3.— (a) *HST* greyscale images of each of the X-ray sources in the three CDFS WFPC2 fields, made by combining the *V* and *I* datasets. The X-ray contours from the smoothed 300 ksec Chandra data are overlaid on each image (with the first three contour levels corresponding to 1, 2, and 3 sigma, and increasing thereafter by a factor of two per contour level). For each image we display a scale bar indicating the FWHM of the ACIS-I PSF. North is to the top and East is to the left.

Fig. 3.— (b) As for Fig. 3a.

Fig. 3.— (c) As for Fig. 3a.

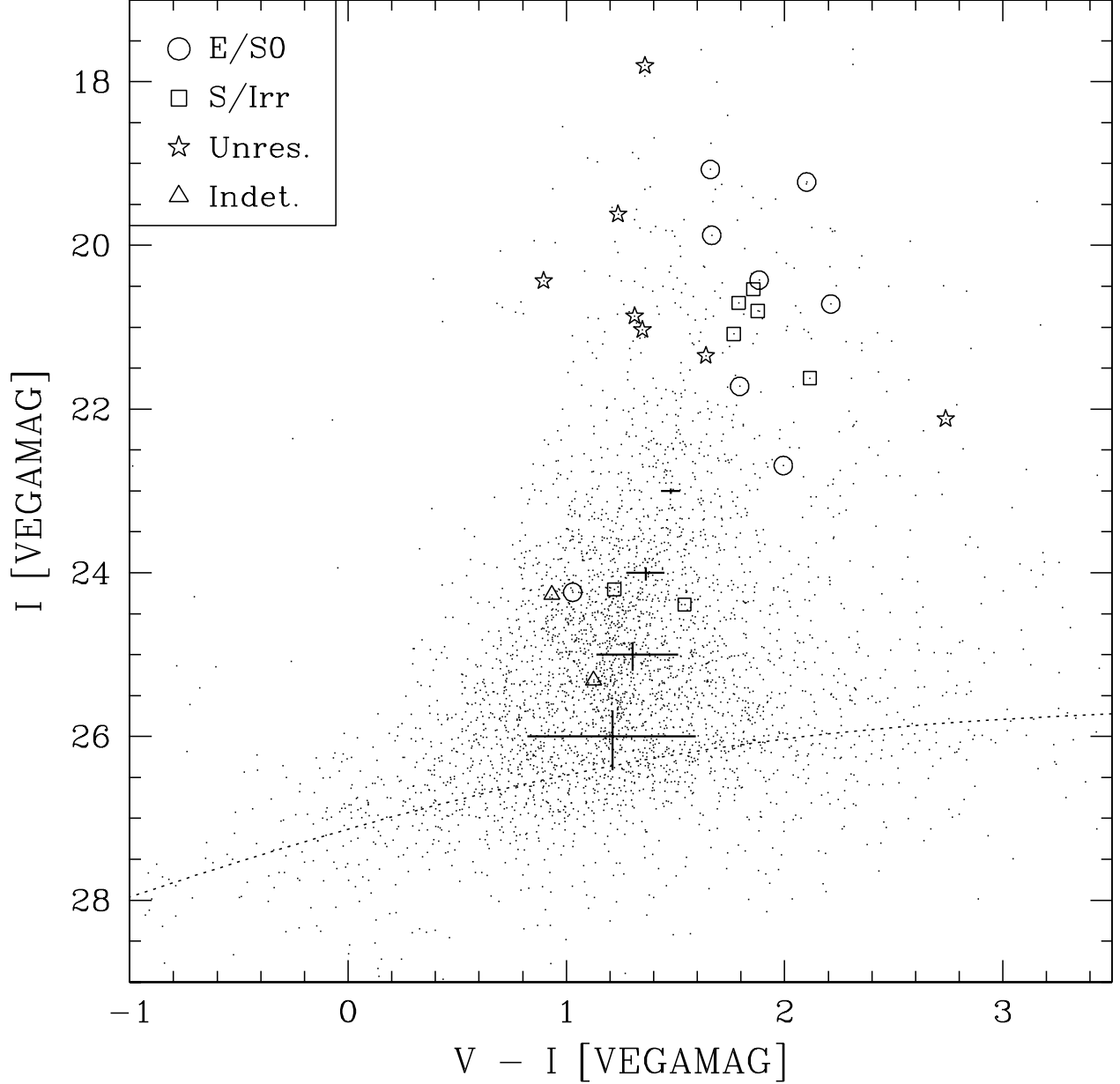


Fig. 4.— Color-magnitude diagram of the 3681 sources (small dots) with both V and I detections in the three WFPC2 fields of this study. Sources with X-ray emission detected in the 300 ksec CDFS image are flagged with larger symbols according to their optical morphology: resolved galaxies of types S0 and earlier (circles); resolved galaxies of types Sa and later (squares); unresolved sources (stars); and indeterminate (triangles). We indicate the catalog completeness limit (dotted line) as well as photometric error bars for sources with $I = 23, 24, 25, 26$ at the median color for the respective magnitude.

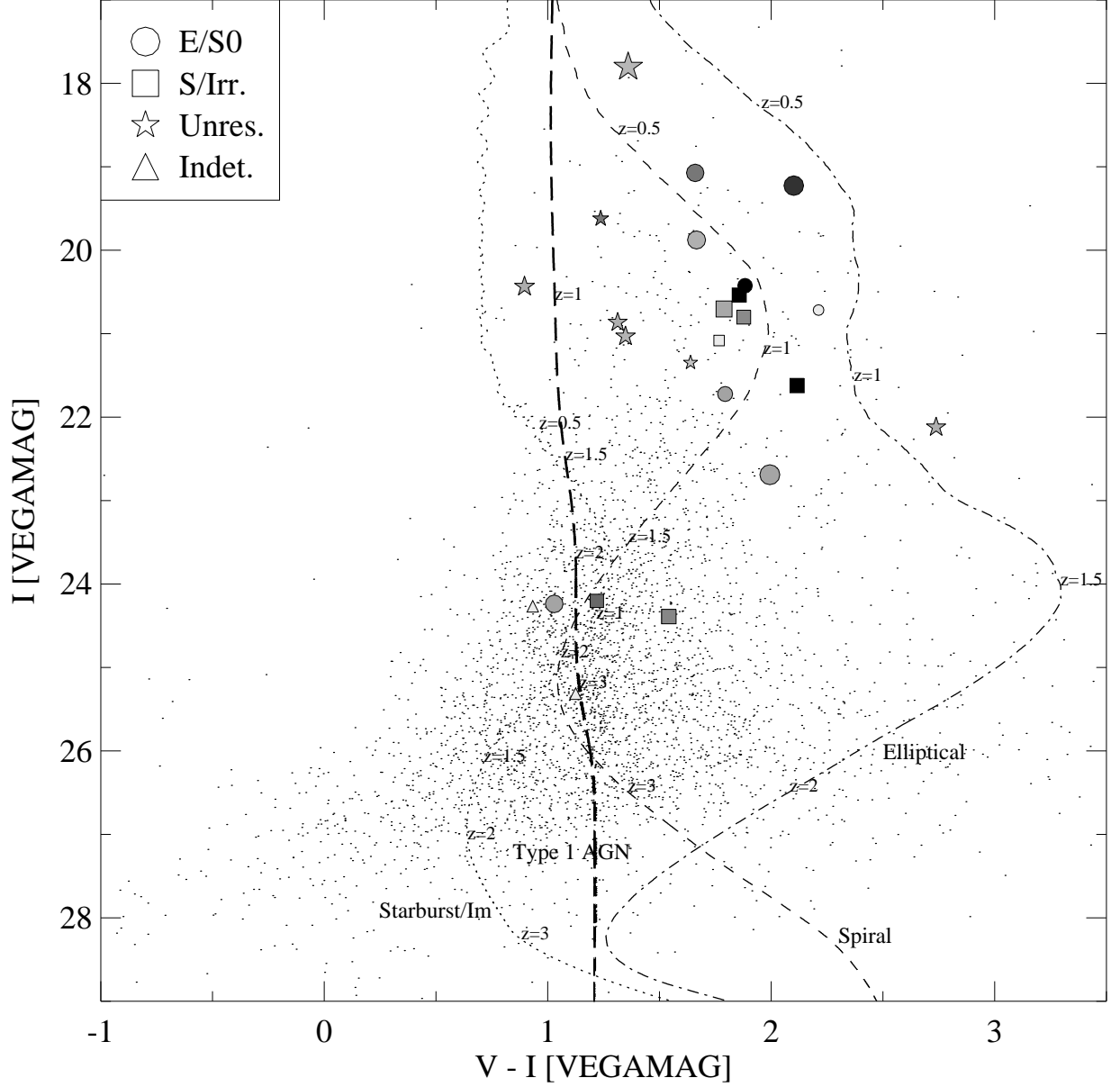


Fig. 5.— Color-magnitude diagram for all sources, showing tracks for elliptical, spiral, starburst/irregular and Type 1 AGN template galaxy SEDs as a function of redshift; see text for further details. Symbols for X-ray detected sources are the same as in Figure 4, except that additional information is contained in their size which now indicates total X-ray flux, while their shading represents X-ray hardness ratio (ranging from white to black for $HR = -1$ to $HR = +1$ respectively).

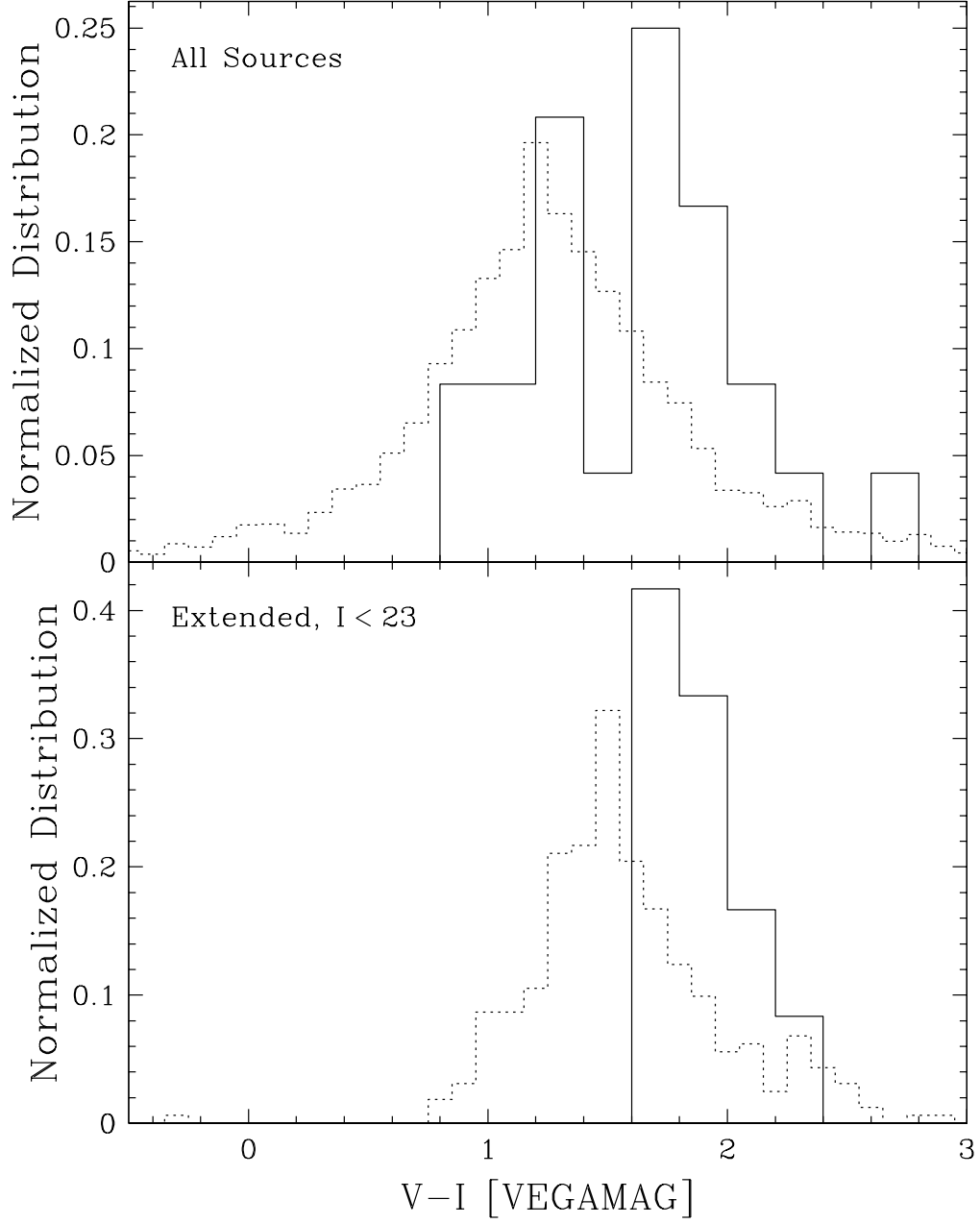


Fig. 6.— Color histograms of *CXO* sources (solid; 0.2 mag bins) versus the entire field (dotted, 0.1 mag bins). The upper plot shows all sources, while the lower plot shows the subset of bright extended sources ($I < 23$, $\eta_V < 0.2$). The histograms are all normalized by bin size and sample size.

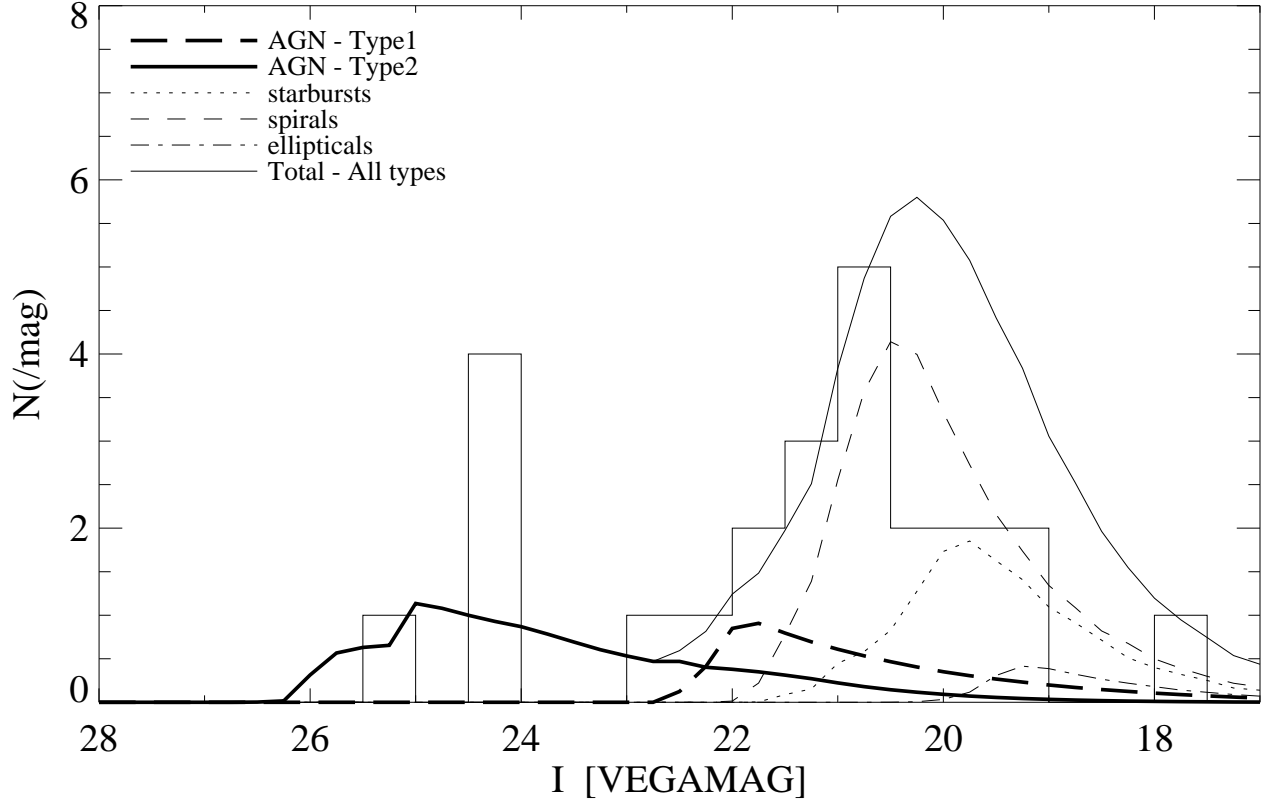


Fig. 7.— Histogram of the I magnitude of the sources with detected X-ray emission, showing the contribution of various different classes of objects. Note in particular that the spirals, ellipticals, and Type 1 AGN are all relatively bright, while the Type 2 AGN are the only ones with a distribution that is peaked fainter than $I \sim 23$.

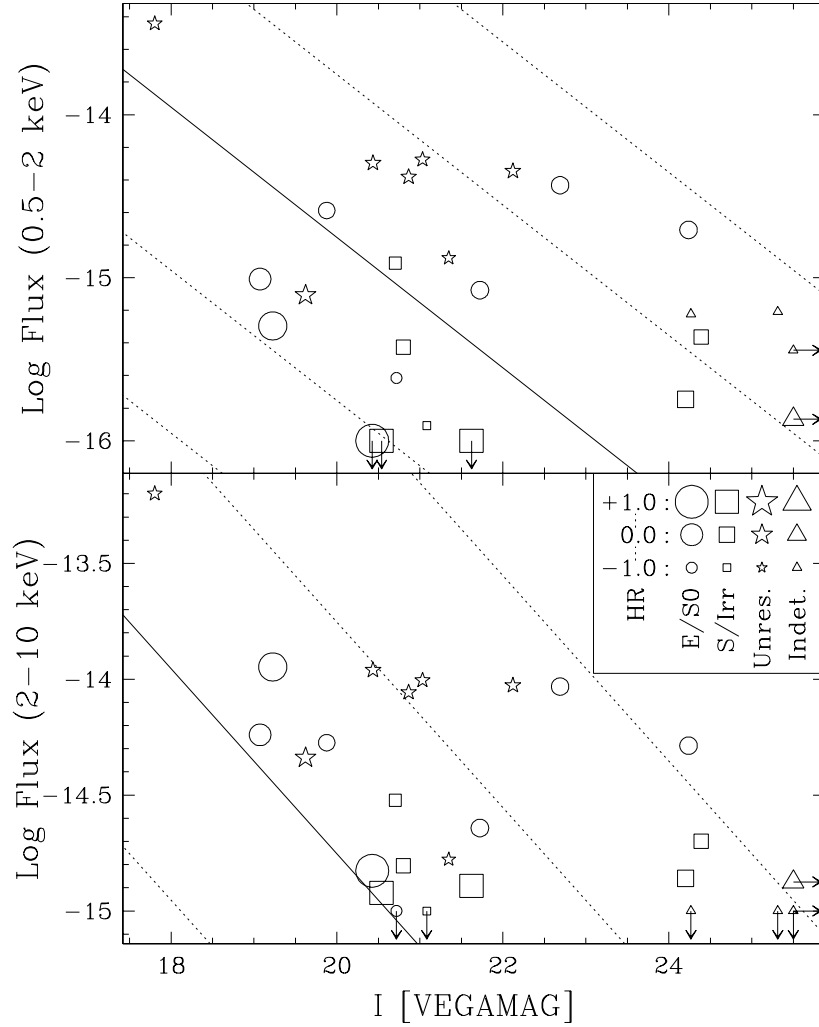


Fig. 8.— I magnitude versus derived X-ray flux at $0.5 - 2$ keV (upper) and $2 - 10$ keV (lower) for all CDFS 300 ksec sources. The different symbols represent optical morphology, as described in Figure 4, and their sizes represent X-ray hardness ratio (legend at right center; see text for definition). In the upper plot, sources detected only in hard X-rays ($2 - 10$ keV) are shown with upper limits given the soft X-ray detection limit of 10^{-16} erg s $^{-1}$ cm $^{-2}$. In the lower plot, sources detected only in soft X-rays ($0.5 - 2$ keV) are shown with upper limits given the hard X-ray detection limit of 10^{-15} erg s $^{-1}$ cm $^{-2}$. In both plots, *CXO* sources without *HST* counterparts are shown with 3σ upper limits in I . The solid line across each plot represents $F_X/F_I = 1$ assuming the conversion I -band 0 mag = 1.762×10^{-7} erg s $^{-1}$ cm $^{-2}$. The dotted lines are spaced at 1 dex intervals in F_X/F_I .

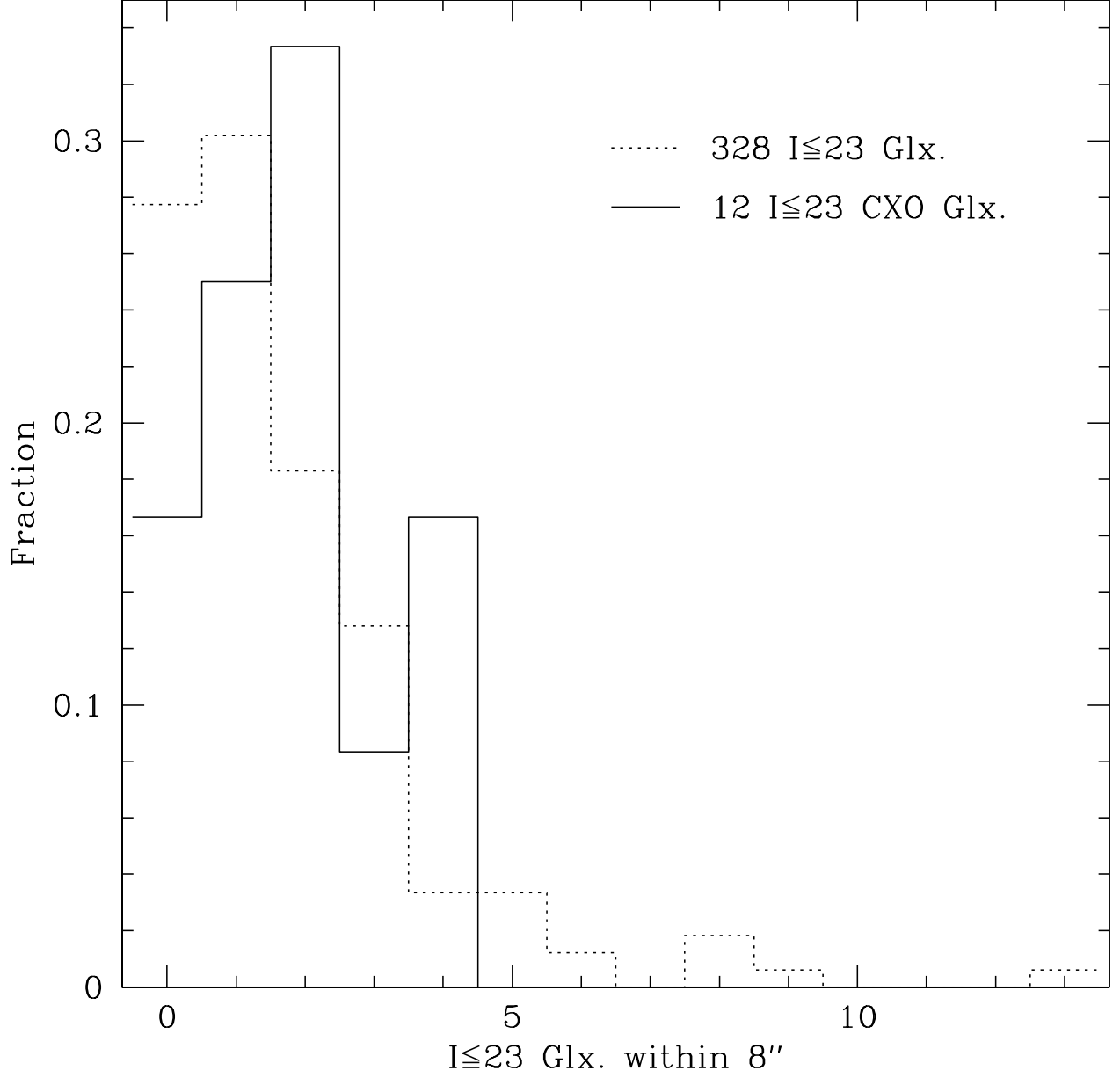


Fig. 9.— Histogram of the number of nearby ($<8''$) $I < 23$ galaxies appearing around the 328 galaxies in our catalog with $I < 23$ (dotted) and around the subset of 12 $I \leq 23$ galaxies detected by *CXO* (solid). The histograms are normalized by the sample sizes.

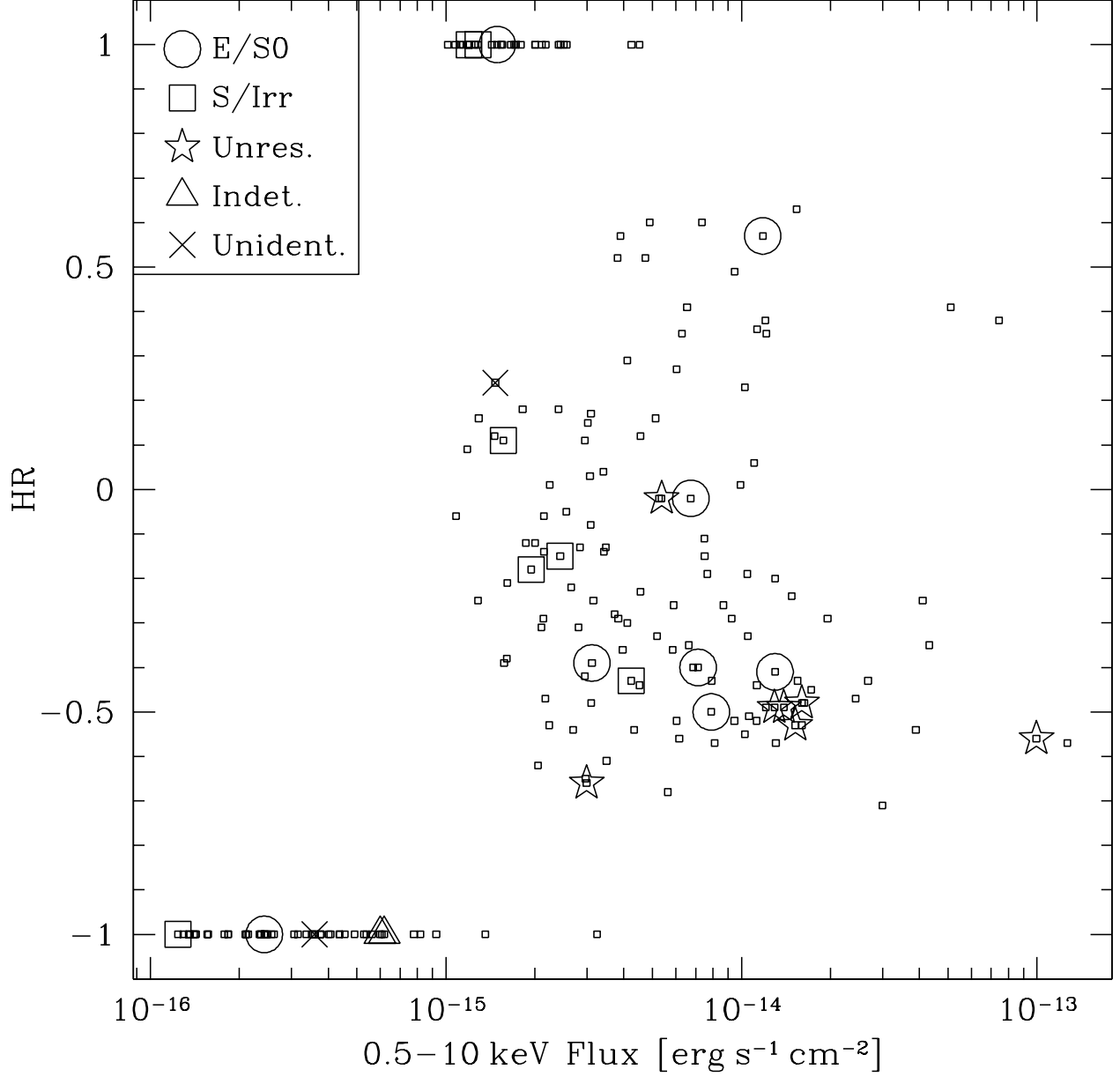


Fig. 10.— Hardness ratio versus 0.5 – 10 keV flux for all *CXO* sources detected in the 300 ksec CDFS image (small squares). The larger symbols denote the morphologies of the optical counterparts within the three *HST*/WFPC2 fields of this study (see legend at upper left). Note the two *CXO* sources lacking optical counterparts (cross symbols).

Table 1. Observations Catalog

ID	α_{J2000}	δ_{J2000}	UT Date	Filter	N_{exp}	T_{tot} (s)
CDFS1	03 32 28.21	−27 45 54.19	2000 Jul 22,23	F606W	8	3700
				F814W	8	5800
CDFS2	03 32 07.01	−27 46 36.19	2000 Jul 23	F606W	8	3700
				F814W	8	5800
CDFS3	03 32 12.11	−27 43 03.19	2000 Jul 27	F606W	8	3700
				F814W	8	5800

Note. — Right ascension α in hours, minutes, and seconds of time. Declination δ in degrees, minutes, and seconds of arc.

Table 2. Properties of CDFS (300 ksec) WFPC2 Counterparts

CDFS ID	$(\Delta\alpha, \Delta\delta)^a$ (arcsec)	V	I	$\log F_{\text{XS}}$ (cgs)	$\log F_{\text{XH}}$ (cgs)	HR	z	Optical Morph.	Spectral Classif.
J033202.5–274601	(−0.51, +0.08)	24.68	22.69	−14.43	−14.03	−0.41	1.613	Ellipt.	AGN–Type 1
J033203.7–274604	(−0.39, +0.30)	21.33	19.23	−15.30	−13.95	+0.57	0.574	S0	NELG
J033204.5–274644	... ^b	> 26.8	> 25.5	−15.44	< −15.0	−1.00
J033205.4–274644	... ^b	> 26.8	> 25.5	−15.87	−14.88	+0.24
J033208.0–274240	(−1.01, −0.65)	22.68	20.80	−15.43	−14.80	−0.18	0.747	Spiral	NELG
J033208.1–274658	(−0.13, −0.16)	25.27	24.24	−14.71	−14.29	−0.40	...	Spiral in CG	...
J033208.3–274153	(−0.26, +0.72)	25.20	24.27	−15.22	< −15.0	−1.00	2.453	Indet.	NELG
J033208.7–274735	(+0.00, +0.00)	19.16	17.80	−13.44	−13.20	−0.56	0.544	Unres.	AGN–Type 1
J033209.5–274807	(+0.00, −0.43)	20.86	19.62	−15.11	−14.34	−0.02	2.817	Unres.	BAL QSO
J033210.6–274309	(+0.00, −0.44)	24.86	22.12	−14.35	−14.03	−0.49	2.0?	Unres.	NELG
J033211.0–274343	(−0.02, −0.82)	22.39	20.54	< −16.0	−14.66	+1.00	...	Spiral	BL Lac?
J033211.0–274415	(+0.11, +0.00)	22.38	21.03	−14.28	−14.00	−0.53	1.606	Unres.	AGN–Type 1
J033211.8–274629	(+0.02, +0.41)	25.93	24.39	−15.36	−14.70	−0.15	...	LSB Spiral	...
J033212.3–274621	(−0.45, −0.14)	23.74	21.62	< −16.0	−14.63	+1.00	1.033	Spiral	...
J033213.3–274241	(+0.29, +0.06)	20.73	19.07	−15.01	−14.24	−0.02	0.606	Ellipt., merger?	NELG
J033214.0–274249	(+0.03, −0.22)	22.31	20.43	< −16.0	−14.57	+1.00	0.735	Spiral	NELG
J033215.0–274225	(−0.39, +0.84)	23.52	21.72	−15.08	−14.64	−0.39	...	Ellipt.	...
J033216.8–274327	(−0.13, −0.49)	22.85	21.08	−15.91	< −15.0	−1.00	...	Spiral	...
J033217.2–274304	(+0.34, +0.26)	21.54	19.88	−14.59	−14.27	−0.50	0.561?	Ellipt.	Low S/N
J033226.0–274515	(+0.17, +0.00)	26.44	25.31	−15.21	< −15.0	−1.00	...	Indet.	...
J033228.8–274621	(+0.37, −0.28)	22.93	20.72	−15.61	< −15.0	−1.00	0.750	Ellipt.	NELG
J033230.1–274524	(−0.14, +0.09)	22.99	21.35	−14.88	−14.78	−0.66	2.569	Unres.	AGN–Type 1.5?
J033230.1–274530	(−0.04, −0.09)	21.33	20.43	−14.30	−13.96	−0.48	1.218	Unres.	AGN–Type 1
J033230.3–274505	(+0.00, +0.20)	22.18	20.86	−14.38	−14.06	−0.49	0.291	Unres.	NELG
J033233.1–274548	(+0.00, −0.19)	22.49	20.70	−14.91	−14.52	−0.43	0.362? ^c	Spiral in CG	...
J033233.9–274521	(+0.46, +0.16)	25.42	24.20	−15.75	−14.86	+0.11	...	LSB Irr.	...

^aJ2000 Right Ascension α and Declination δ offsets ($HST-CXO$), in arcsec.

^bNo counterpart within $2''$ of CXO position; V , I mags are 3σ upper limits.

^cRedshift of adjacent bright elliptical in compact group.

This figure "fig1a_color_full.jpg" is available in "jpg" format from:

<http://arXiv.org/ps/astro-ph/0105271v1>

This figure "fig1b_color_full.jpg" is available in "jpg" format from:

<http://arXiv.org/ps/astro-ph/0105271v1>

This figure "fig1c_color_full.jpg" is available in "jpg" format from:

<http://arXiv.org/ps/astro-ph/0105271v1>

This figure "fig3a_grey_20x20.jpg" is available in "jpg" format from:

<http://arXiv.org/ps/astro-ph/0105271v1>

This figure "fig3b_grey_20x20.jpg" is available in "jpg" format from:

<http://arXiv.org/ps/astro-ph/0105271v1>

This figure "fig3c_grey_20x20.jpg" is available in "jpg" format from:

<http://arXiv.org/ps/astro-ph/0105271v1>